Electronic transport properties of nanographite ribbon junctions

Katsunori Wakabayashi*
Department of Quantum Matter Science, Graduate School of Advanced Sciences of Matter (ADSM), Hiroshima University, Higashi-Hiroshima 739-8527, Japan
and Department of Physical Electronics, Faculty of Engineering, Hiroshima University, Higashi-Hiroshima 739-8527, Japan
(Received 8 March 2001; published 11 September 2001)

The electronic transport properties through junctions connecting nanographite ribbons of different or same width are investigated by means of the Landauer-Büttiker approach using a tight binding model. Graphite ribbon with zigzag boundary has a single conducting channel of edge states in the low-energy regime. The electrical conductance as a function of the chemical potential shows a rich structure with sharp dips of zero conductance. This perfect reflectivity originates from twofold degenerate resonant levels, i.e., flux states visible in the formation of strong current-current correlation with a Kekulé-like vortex pattern. At each energy of conductance-zeros, this degeneracy yields the formation of standing waves in the scattering region of the junctions. The origin of zero-conductance resonances is also discussed by the standard scattering matrix approach, and the similarities between the nanographite ribbon junctions and the asymmetric Aharanov-Bohm ring connected to current leads are pointed out. Since the zero-conductance resonances are connected with the time-reversal symmetry of the system, the application of a magnetic field removes these zero-conductance dips, yielding a pronounced negative magnetoresistance.

DOI: 10.1103/PhysRevB.64.125428 PACS number(s): 72.10.−d, 72.80.Rj, 73.23.−b, 73.20.−r

I. INTRODUCTION

Electron transport through nanometer-sized structures is one of the recent fundamental issues in the mesoscopic and nanoscopic physics.[1] The motivation for this type of study is the development of atomic or molecular scale electronic devices, which not only could increase the device density in an integrated circuit enormously, but also the operation principles of a transistor could be fundamentally different from ordinary electronic devices.[2] Recently, nanometer-sized carbon systems such as carbon nanotubes[3,4] have attracted much attention for the possibilities as carbon-based molecular-electronic devices. In nanometer-sized carbon systems, the geometry of sp^2 carbon networks has much influence on the electronic states near the Fermi level. Studies with scanning tunneling microscopy and spectroscopy have confirmed the connection between the electronic states of the single wall carbon nanotubes (SWCN's) and their geometry.[5] Recent experiments can provide the electrical transport measurement of individual SWCN's,[6–10] the observation of quantized conductance of multi-walled carbon nanotubes,[11] and the fabrication of SWCN junctions sandwiched by magnetic or superconducting materials.[12,13] These experiments initiated theoretical studies devoted to effects of nonmagnetic impurity,[14] electron correlation,[15] and topological defects.[16–20]

Not only the closed carbon molecules such as carbon nanotubes and fullerene molecules, but also systems with open boundaries also display unusual features connected with their shape. Fujita and co-workers have pointed out that the existence of graphite edges strongly affects the π-electronic states in nanometer-sized graphite fragments (nanographites).[21] There are two basic edge shapes in graphite, armchair and zigzag. For the model of graphite ribbons, one-dimensional graphite lattices of finite width,[21–34] it was shown that ribbons with zigzag edges (zigzag ribbon) possess localized edge states with energies close to the Fermi level.[21–25] These edge states correspond to the non-bonding molecular orbital as can be seen by examining the analytic solution for semi-infinite graphite with a zigzag edge. In contrast, edge states are completely absent for ribbons with armchair edges. The edge states were analyzed in terms of nearest-neighbor tight binding models[21–25] and density functional approach.[35] We have also pointed out that the edge states play important roles in magnetic properties in nanometer-sized graphite systems, because of their relatively large contribution to the density of states at the Fermi energy.[21–25,27]

In this paper, we present the electron transport properties through nanographite ribbon junctions, in which we find that the edge states play important roles not only for magnetic properties, but also for electron transport phenomena. Because of the nonbonding character of edge states, a single edge state cannot contribute to the electron transport. However, in zigzag ribbons, the edge states can provide a single-channel for electron conduction in the low-energy region, due to the bonding and antibonding interaction between two edge states which overlap from both edges. In order to analyze the electronic transport properties responsible for edge states, we consider the nanographite ribbon junction systems which connect two zigzag ribbons with different or same width. The electrical conductance of the junctions is calculated through the Landauer-Büttiker formula based on a simple tight binding model, in which the conductance is written in terms of the transmission coefficient.[1,36–38] We calculate the transmission coefficient through the junctions in terms of the recursive Green's function method which provides high efficiency and accuracy for numerical calculations.[39,40]

Conductance of nanographite ribbon junctions as a function of the Fermi energy shows rich structures in the energy region corresponding to single channel transport.[23,41] The re-

markable feature in the behavior of the conductance is the appearance of sharp zero-conductance dip structures corresponding to total reflection resonances. These conductance zeros are associated with the presence of resonant localized states in the junction region which resemble flux states in the sense that they show a strong current-current correlation with a Kekulé-like vortex pattern. The resonant state is a standing wave resulting from the superposition of two flux states which are the time reversed of each other. We also show that zero-conductance dips can be well interpreted in terms of the result of an asymmetric Aharanov-Bohm (AB) ring connected to current leads. Since these resonances are intimately connected with the time-reversal symmetry of the system, the application of a magnetic field removes the conductance zeros, yielding a pronounced negative magnetoresistance. In this paper, we emphasize that edge states in nanographite ribbons lead to electronic transport properties distinctively different from those found in usual quantum wires or carbon nanotubes.

We organize this paper as follows. In Sec. II, we briefly introduce our model for the calculation for the electrical conductance of nanographite ribbon junctions. In Sec. III, we analyze the problem of the nanographite ribbon junctions and their zero-conductance resonances from the behavior of electron waves and electric currents. The response of the flux states to the net current through the junctions is also discussed. In Sec. IV, we show the connection between the transport properties of nanographite ribbon junctions and the asymmetric AB ring connected to current leads, on the basis of the standard scattering matrix approach. The summary and discussion are given in Sec. V. The conclusions are presented in Sec. VI.

II. MODEL

We use the Landauer-Büttiker formula[1,36–38] in order to evaluate the conductance through nanographite junctions. In order to describe the π-electronic states of nanographite ribbon and junctions, we use a nearest-neighbor tight-binding model, which is successfully used in the studies of fullerene molecules, carbon nanotubes, and carbon-related materials.[42–44] The tight-binding Hamiltonian is defined by

$$H=\sum_{i,j} t_{i,j}|i\rangle\langle j|, \tag{2.1}$$

where $t_{i,j}$ is transfer integral and $|i\rangle$ is a localized orbital on site i. Throughout this paper, the transfer integrals are set to t between all the nearest neighbor sites and otherwise to 0 for a simplicity, because we aim at the intrinsic difference in the transport properties originating from the topological nature of systems. The transfer integral t is used as the unit of the energy, and estimated about 3.03 eV.[44]

The magnetic field $\boldsymbol{B}$ perpendicular to the graphite plane is incorporated in the transfer integral t_{ij} by means of the Peierls phase[45] defined as $t_{ij}\rightarrow t_{ij}e^{i2\pi\theta_{i,j}}$, where $\theta_{i,j}$ is given by the line integral of the vector potential from site i to site j,

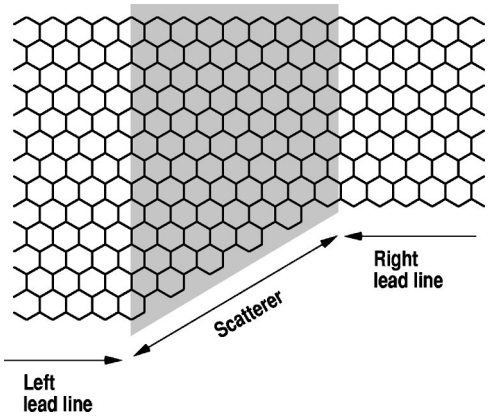

FIG. 1. An example configuration of nanographite ribbon junctions. The shaded central region is the scatter. Lead lines (zigzag ribbons) are attached on the both of the scatter.

$$\theta_{i,j}=\frac{e}{ch}\int_i^j d\boldsymbol{l}\cdot\boldsymbol{A}. \tag{2.2}$$

The magnetic flux through the area S in units of the flux quantum $\Phi_0=ch/e$ is

$$\frac{1}{\Phi_0}\int d\boldsymbol{S}\cdot\boldsymbol{B}=\frac{e}{ch}\oint dl\cdot A=\sum_{\text{area }\mathbf{S}}\theta_{i,j}. \tag{2.3}$$

We define the magnitude of the magnetic flux passing through a single hexagon ring of graphite in the unit of the quantum flux as θ. The θ is given as $\theta=BS_{\text{hex}}/\Phi_0$, where $B=|\boldsymbol{B}|$ and $S_{\text{hex}}=3\sqrt{3}a_0^2/2$. The S_{hex} is the single hexagon ring has the area, and $a_0=1.42$ Å is the lattice constant of graphite. Then $\theta=1$ corresponds to 7.9×10^4 T. The cyclotron radius (magnetic length), l_m, is given by

$$l_m=\sqrt{\frac{c\hbar}{eB}}. \tag{2.4}$$

In ribbon-shaped systems, the ratio between the width of a ribbon and cyclotron diameter effectively characterizes the electronic states of ribbon in a magnetic field. Therefore, we define the ratio between the ribbon width and the cyclotron diameter as the effective magnetic field $\tilde{B}$ for a convenience, which is given by

$$\tilde{B}=\left(\frac{W}{d}\right)^2, \tag{2.5}$$

where $d=2l_m$ and W means the ribbon width in the units of the lattice constant defined for zigzag ribbons as[23,25] $W=3Na_0/2-a_0$, where N is the number of zigzag lines in zigzag ribbons. Note that $\tilde{B}$ is proportional to B.

An example of the nanographite ribbon junctions is depicted in Fig. 1. The shaded central region corresponds to the scattering region, and the zigzag ribbons of the left and right parts correspond to lead lines. We assume that the electron wave comes in out of the νth channel of the left lead line and transmit, passing through the scatter of central region, to the μth channel of the right lead line with the transmission co-

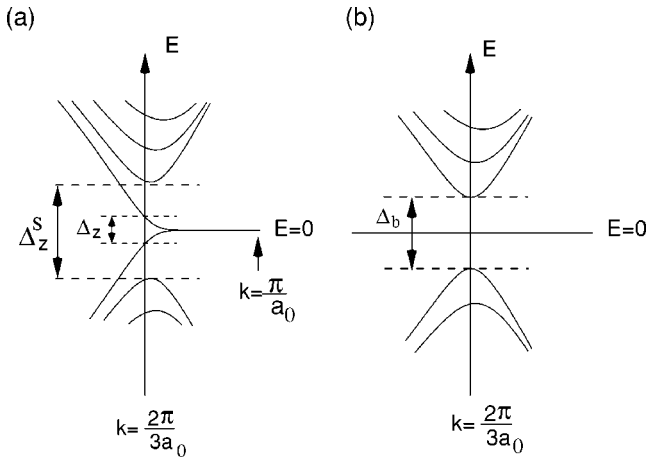

FIG. 2. The band structure near $E=0$ of (a) zigzag ribbons and (b) bearded ribbons.

efficient $t_{\mu\nu}$. Since the transmission probability $T_{\mu\nu}$ is the square of transmission coefficients, i.e., $T_{\mu\nu}=|t_{\mu\nu}|^2$, electrical conductance can be evaluated by the Landauer-Büttiker formula

$$G(E)=\frac{e^2}{\pi\hbar}\sum_{\mu,\nu}T_{\mu\nu}(E)=\frac{e^2}{\pi\hbar}\sum_{\mu,\nu}|t_{\mu\nu}(E)|^2. \quad (2.6)$$

Here $e^2/\pi\hbar$ is quantum conductance. In this paper, we use the quantum conductance as the unit of conductance. The transmission coefficients and the electron waves in the scatterer are calculated in terms of the the recursive Green function method, which provides high efficiency and accuracy for numerical calculations.[39,40]

III. SINGLE-BARRIER NANOGRAPHITE RIBBON JUNCTIONS

A. Design of single-barrier nanographite ribbon junctions

The junctions which we will discuss here are build from nanographite ribbons. We first summarize a few facts of the basic building blocks of these junctions, the zigzag ribbon and the so-called bearded ribbon.[21,23,25,46,47].

The main ribbon structure we will consider is the one with zigzag edges. The zigzag ribbons are metallic for arbitrary ribbon width with an energy dispersion near $E=0$ as shown in Fig. 2(a). There is a partly flat band at $E=0$ which is a special feature of the zigzag edge in graphite. It originates from edge states which have a nonvanishing amplitude of the wave function on only one of the two sublattices. Consequently it has nonbonding character and would not disperse at all. However, in a zigzag ribbon of finite width, the two edges provide this kind of edges states belonging to different sublattices. The finite overlap of the edge state from both sides yield a mixing into bonding and antibonding configuration. Because the overlap depends continuously on the momentum along the ribbon, it leads to finite dispersion for these states with the peculiar form shown in Fig. 2(a). Note that the overlap is enhanced as k deviates from π/a_0 where the overlap is zero, because the penetration depth of the edge states increases and diverges at $k=2\pi/3a_0$. Naturally the dispersion depends on the ribbon width N (number of zigzag lines from one side to the other), and can be approximated by

$$E_k=\pm 2tND_k^{N-1}\left[1-\cos\left(\frac{ka_0}{2}\right)\right], \quad (3.1)$$

for k close to π/a_0, where $D_k=2\cos(ka_0/2)$. Thus the overlap of the two edge states gives rise to a single conduction channel for energies close to $E=0$. Only at exactly $E=0$ the vanishing group velocity yields no conducting channel. Apart from the $E=0$, there are many higher energy states providing multichannel conductance. We define the single-channel energy region as the energy gap to the lowest of multichannel states Δ_z^s in Fig. 2(a)

$$\Delta_z^s=4t\cos\left[\frac{N-1}{2N+1}\pi\right]. \quad (3.2)$$

In the following our main interest lies in the single-channel region.

Next let us introduce the so-called bearded ribbon. This corresponds to a zigzag ribbon where on one side additional bonds (beard) is attached to edge. Also the bearded edge possesses a zero-energy nonbonding state. The main difference to the ordinary zigzag ribbon lies in the fact that here the edge states on both sides (one zigzag and one bearded edge) are now located on the same sublattice. Hence, their overlap will not mix them and we do not end up with a bonding and antibonding configuration. As shown in Fig. 2(b) the edge state provide an entirely flat band. This band does not contribute to transport, since the group velocity is zero. We may consider this ribbon as insulating within the energy range defined by the gap

$$\Delta_b=4t\cos\left[\frac{N}{2N+2}\pi\right]. \quad (3.3)$$

Note that the bearded ribbon is not considered as a realistic form of the nanographite ribbons. We will use it in the following as a unit which will allow us to create a nontrivial ''toy junction.''

The main junction we will consider here is made of two regular zigzag ribbons as lead lines on the left (L) and right (R) hand side, interrupted by an intermediate bearded ribbon (M), all of the same width. This device can be viewed as a metal-insulator-metal junction [see Fig. 3(a)], and we will refer to it as junction I in the following. This junction is defined by the width of the leads N and the number of attached bonds l of the bearded region M. The other two examples which we analyze are junctions connecting lead lines L and R of different width as shown in Figs. 3(b) and 3(c). The intermediate region M for junction II includes a tilted zigzag edge and for junction III a tilted armchair edge. These latter two designs may be more feasible as experimental devices. Note that the dimensions of the junction region in junction II and III is entirely determined by the width of the lead lines, N_L and N_R.

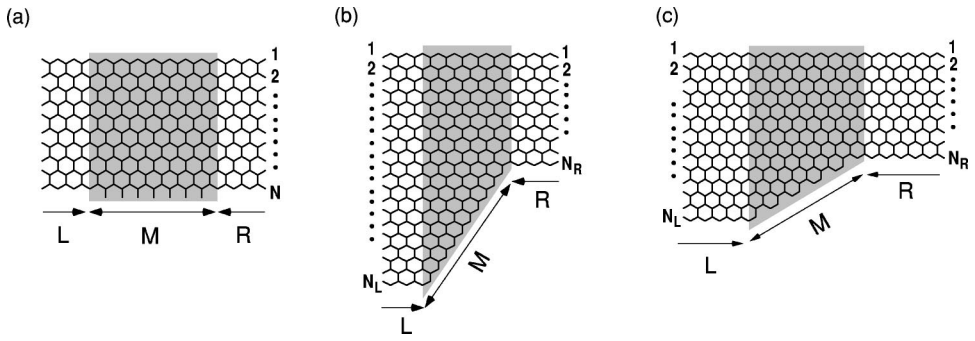

FIG. 3. The structure of junction (a) I, (b) II, and (c) III.

B. Fermi energy dependence of conductance

We would now like to discuss the energy dependence of the conductance $G(E)$ of the junctions I–III. The energy may be considered as the chemical potential which could be adjusted by a gate underneath the junction. The energy $E=0$ corresponds to the undoped system which is half-filled. As mentioned above we use an iterative Green's function scheme to evaluate the transmission probabilities.

In Fig. 4(a), the Fermi energy dependence of the ballistic conductance for the junction I with $N=20$ for the whole energy region, where the number of attached bonds is 0, 1, and 3. Since the system with $l=0$ is a perfect conductor, the ballistic conductance is proportional to the number of conducting channels at the Fermi energy, i.e., the number of subbands at the Fermi energy. The conductance has a clear step feature as a function of the Fermi energy. With increasing number of attached bonds, the conductance decreases due to the backward scattering. In the multichannel energy region the structure of the function $G(E)$ is rather smooth, however in the single-channel region near $E=0$ the conductance has strong features for $l\neq 0$. Since in realistic systems the low-energy region close to $E=0$ which is the Fermi energy for undoped system is most important, we shall draw attention to the behavior of the conductance in the low-energy region. The $G(E)$ of junction I for the single-channel region $|E|<\Delta_b/2$ is shown in Figs. 4(b) and 4(c) with log scale for the Fermi energy. The characteristic feature is the appearance of zero-conductance dips at the specific values of E where the system shows complete back scattering. The number of dips increases with increasing the number of the attached bonds, and simultaneously the maximum height of the conductance decreases. Interestingly, even one-attached bond makes a zero conductance dip. We should note that near the bottom of the valence bands (the top of the conduction bands) which is also a single-channel region the dip structures of zero conductance does not appear. Since the bottom of the valence bands (the top of the conduction bands) has the character of ordinary free electrons, the appearance of the zero-conductance near $E=0$ dips is related to the topology of the lattice and the electron spectrum around $E=0$. We should remark that the conductance of junctions connecting two nanotubes with different circumference does not show this type of dip structures.[19]

Next we show the behavior of conductance for junctions II and III in Figs. 5 and 6, respectively. In Fig. 5, the Fermi energy dependence of the conductance in junction II for (a) the whole energy range, (b) the single conducting channel region, and (c) single conducting channel region with log-scale are displayed. Here we define the single-channel region as $|E|<\Delta_b(N_L)/2$, where both leads have a single conducting channel [$N_L>N_R$ implies $\Delta_b(N_L)<\Delta_b(N_R)$]. Similarly, in the Fig. 6, we show the Fermi energy dependence of the conductance in junction III. For both types of junctions, we fix the width of the left zigzag ribbon at $N_L=20$, the width of the right zigzag ribbon is changed as $N_R=16,14,10$. When N_L is equal to N_R, the system is a perfect conductor, so that the conductance is a step function of the Fermi energy. Since the maximum number of conducting channels is equal to the

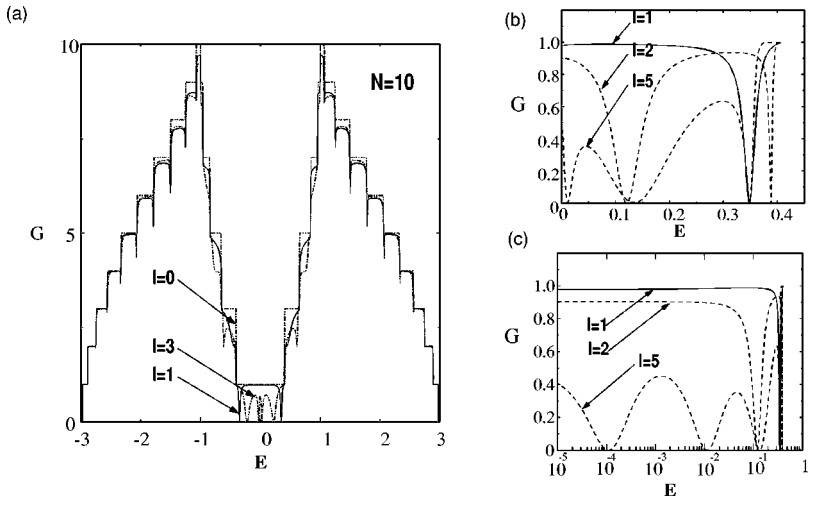

FIG. 4. The Fermi energy dependence of the transmission probability of the junction I for (a) the whole energy region, (b) the energy region of single conducting channel, and (c) with log-scale for the Fermi energy.

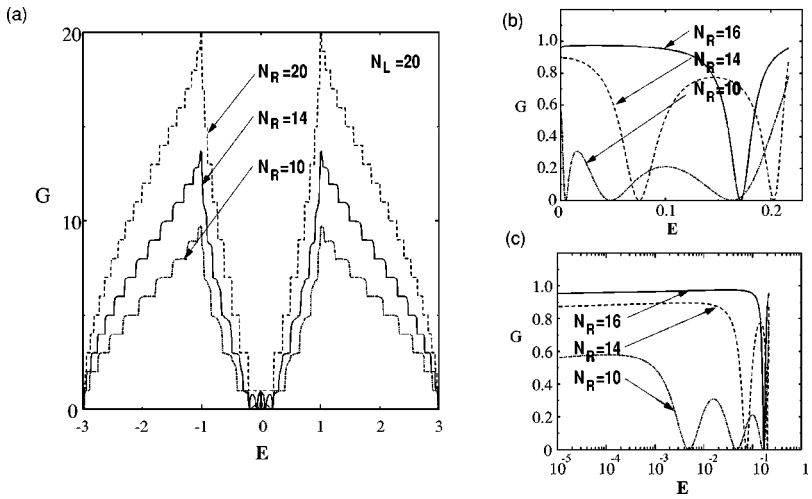

FIG. 5. The Fermi energy dependence of the transmission probability of the junction II for (a) the whole energy region, (b) the energy region of single conducting channel, and (c) with log-scale for the Fermi energy.

width of the lead lines, the maximum value of the conductance is equal to the width of the right zigzag ribbon, so that the conductance decreases with decreasing the width of right zigzag ribbon in the multichannel region. Interestingly, although we can find sharp dips in the multichannel region of $|E|>1$ for the junction I, we cannot find such structures for junction II and III. Now we turn to the low-energy transport properties. The behavior of the conductance of the junction II and III is qualitatively same in the multichannel region. However, in the single-channel region near $E=0$, the behavior of the conductance of junctions II and III is quite different. The conductance of junction III is smooth even in the single-channel region, but for junction II dip structures analogous to the junction I appear.

In junction II, with increasing the length of the M region, the number of the zero-conductance dips increases and the height of the conductance decreases. The tilted edge in junction II supports an edge state which, similar to the bearded ribbon, lies on the same sublattice as the edge state on the other side of the ribbon. Again with increasing the length of the M region, the conductance is lowered because of the enhanced reflection of the electron wave.

Considering the conductance the region around $E=0$ then we find that junction II behaves very similar to junction I, while junction III belongs to another class. The property common to junction I and II is that the junction regions support edge states whose wave function resides on both sides on the same sublattice. It is easy to see that the tilted zigzag edge indeed switches the sublattice in junction II. On the other hand, in junction III the tilted edge has armchair structure and does not have any edge state.

C. Behavior of electron waves

The presence of edge states in the junction region seems to be essential for the zero-conductance dips. The analysis of the electron wave functions shows that the states at energies corresponding to zero-conductance dips form standing waves in the junction, corresponding to resonant states. We present here the result for junction I with $N=20$ and $l=6$ where we visualize the wave function for three energies in Fig. 7. We restrict to the wave function on only on the sublattice carrying the edge state in the junction region. Here a clear structure of a standing wave emerges [note that in Figs. 7(b)–7(d) we encoded the amplitude of the wave function by the size of the circles and the sign by black and white for positive and negative, respectively]. Obviously, different energies are associated with different numbers of nodes or hills of the standing wave which we may use to label them. Note that the longer the junction the more standing waves fit into it and the more zero-conductance dips should occur in accordance with our observation. Furthermore we would like to draw the at-

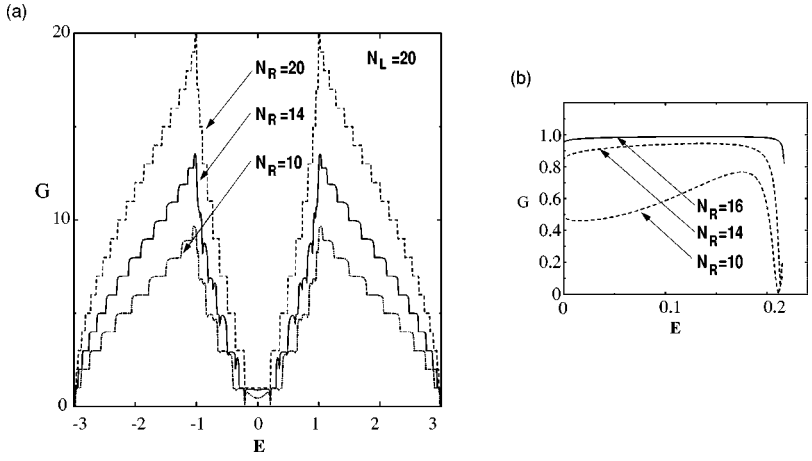

FIG. 6. The Fermi energy dependence of the transmission probability of the junction III for (a) the whole energy region and (b) the energy region of single conducting channel.

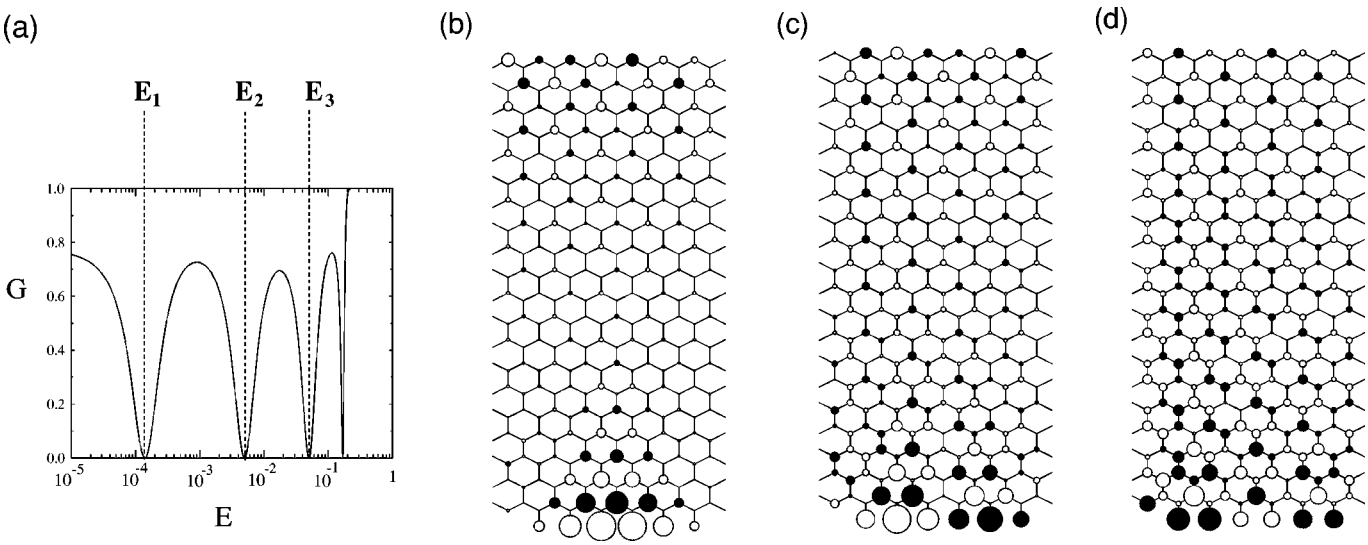

FIG. 7. (a) The energy dependence of the conductance of the junction I with $N=20$ and $l=6$. The electron waves of this junction at the energy (b) E_1, (c) E_2, and (d) E_3. Here the radius of a circle and the black and white of a circle means the amplitude and sign of the electron waves.

tention to the fact that the wave function extends further into the ribbon the higher the energy. This will be important when we discuss the magnetoresistance phenomenon later. As both edges of the junction region develop a standing wave, where the one on the bearded side is clearly more pronounced. Analyzing their symmetry properties we realize that the parity under exchanging L and R is opposite for the standing waves on the two sides. Consequently, we may conclude that the zero-conductance dip is a resonance phenomenon involving the interference of two states of opposite parity. We will see below that this is indeed a crucial feature for the presence of zero-conductance dips.

A similar analysis is possible for junction II where we also can observe standing waves as a resonant state at the energy of zero conductance, especially at the tilted zigzag edge. The overall structure is, however, more difficult to analyze than in our toy junction I. The tilted armchair edge of junction III does not provide the environment for a standing edge state, so no zero-conductance dips are expected with single-channel region.

Thus, the appearance of zero conductance can be attributed to the formation of standing waves in the junction. Hence the M region of the junctions plays a role of single potential barrier for electron tunneling. In general, when the length of the potential barrier gets longer, the energy of the long-wavelength standing waves in the M region become smaller. This is the reason why the number of zero-conductance dips increases with increasing the length of the M region. Of course, if the length of the M region gets longer, the electron transmission is reduced, resulting in the decrease of the height of the conductance.

D. Large induced current vortex

The appearance of the zero-conductance resonances can be understood by the formation of standing waves due to the interference effects between the incident and scattered electron waves. This interference effects produce the additional structure in the spatial distribution of the electric currents over the scattering region of the nanographite ribbon junctions. In this section, we draw attention to the spatial distribution of electric currents close to the energies of the zero-conductance dips. For energies close to a zero-conductance resonance, a Kekulé-like vortex pattern appears over the scattering region. The nearly regular pattern reminds of a flux state. We will see that the resonant state responsible for the zero-conductance dip may also be considered as a standing wave due to the superposition of such a ''flux phase'' and its time reversed state.

In order to visualize the spatial distribution of electric currents, we study here bond current distribution. The bond current flowing from site-j to site-i is defined by

$$J_{i,j}=i\frac{et}{\hbar}e^{i2\pi\theta_{i,j}}|i\rangle\langle j|+\text{H.c.}). \tag{3.4}$$

In Fig. 8(a), we show the distribution of the currents for junction I of $N=20$ and $l=6$, at $E=0.049565$. This energy lies immediately below E_2, a zero-conductance resonance shown in Fig. 7(a). The overall currents give rise to a clockwise vorticity. In the junction region we observe a clear triangular Kekulé pattern of the current vortex. Interestingly, the center of the junction region supports large circulating currents while the net current passing through the junction is rather small. We see also that the current pattern rapidly vanishes when we leave the junction region. When we increase the energy slightly above E_2 we find a very similar current distribution pattern in the junction region. While the net current is flowing in the same direction as in the previous case the vortex pattern shows the opposite orientation and also the overall vorticity is reversed. Considering current distribution at an energy far from a resonance, e.g., $E=0.21517t$ with

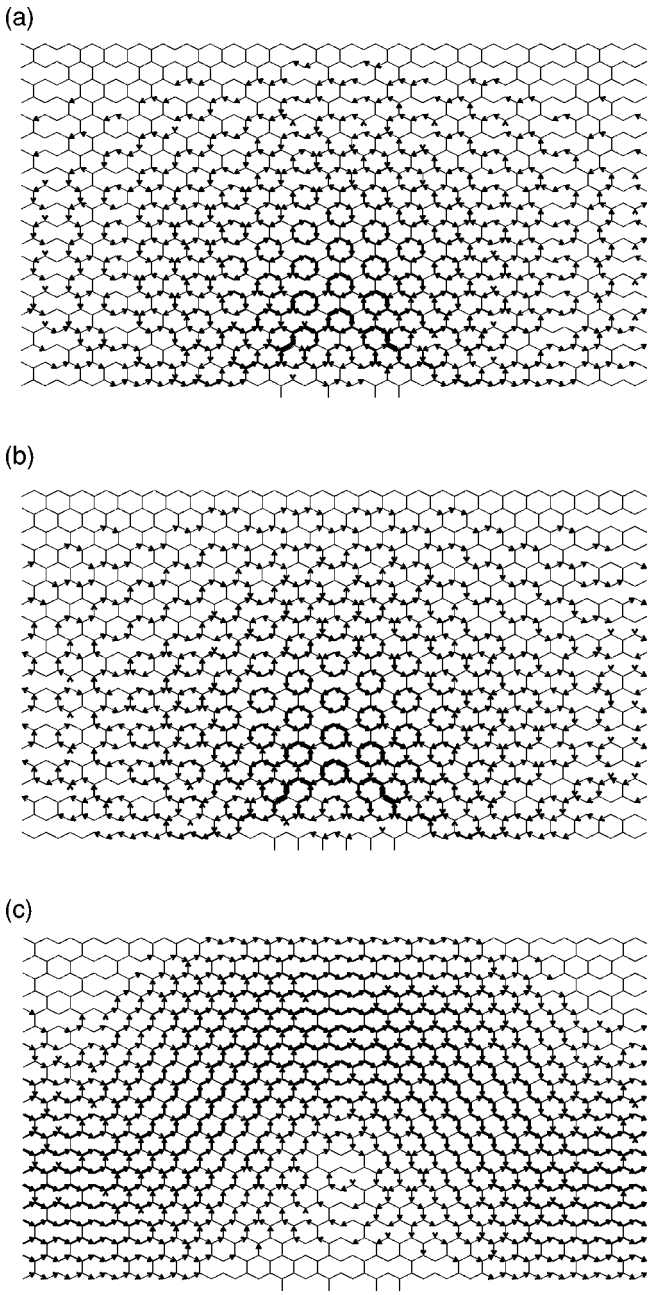

FIG. 8. The distribution of currents in the M region of the junction I with $N=20$ and $l=6$, at (a) $E=0.049565t$ (immediately below E_2), (b) $E=0.050289t$ (immediately above E_2), and (c) $E=0.21517t$ where $G=0.72636$.

$G=0.72636$, we do not observe this type of Kekulé-like vortex pattern, but a more or less laminar flow, as can be seen in Fig. 8(c).

In order to analyze the features of this current vortex pattern in more detail we introduce the local *vorticity* which is defined on the dual (triangular) lattice as the clockwise sum of the currents flowing on the bonds of each hexagonal ring. The local vorticity on the pth hexagonal ring is given by

$$V_p=\sum_{i=1}^{6} I_{i,p}, \tag{3.5}$$

where $I_{i,p}$ means the current on the ith bond of pth hexagonal ring. In order to quantify the total of all circulating currents flowing in the junction, we take an average of $|V_p|$. Thus this quantity V_1 is given by

$$V_1=\langle |V_p| \rangle = \frac{\sum_p |V_p|}{\sum_p 1}. \tag{3.6}$$

Similarly, we also define the total vorticity of the junction V_2 as

$$V_2=\langle V_p \rangle = \frac{\sum_p V_p}{\sum_p 1}. \tag{3.7}$$

This represents the direction of the total circulating current component of the junction. It should be noted that the summation over plaquettes is taken over rings in the junction region M and slightly beyond including several columns of rings in L and, because there is a *proximity effect* of the current vortex pattern, i.e., the components of circulating currents penetrate into both the left and the right lead lines. In Fig. 9, we show the Fermi energy dependence of V_1 and V_2 for the junction I with $N=20$ and $l=6$ in the single conducting channel region. Both V_1 and V_2 vanish at each energy of zero conductance, i.e., not only the total vorticity V_2 disappears, but also no circular currents can be found in each individual plaquette ($V_1=0$). Moreover, the vorticity V_2 changes the sign at each zero-conductance energy point. Note that both V_1 and V_2 vanish in a linear dependence of $E-E_n$ close to the zero-conductance point E_n. The fact that both vorticities go to zero at each zero-conductance energy E_n verifies the claim that the resonant state in the junction region may be also interpreted as a standing wave as the superposition of two flux phaselike states which are connected with each other by means of time reversal operation. This also suggests that the resonance should disappear once time reversal symmetry is explicitly violated, for example, by an external field. As we will show later there is indeed a negative magnetoresistance associated with the zero-conductance dips.

The study of V_p allows us also to observe the formation of the Kekulé-like vortex pattern easily, if we transform V_p into momentum space,

$$F(\boldsymbol{k})=\sum_p V_p \cos(\mathbf{k}\cdot\mathbf{r}_p), \tag{3.8}$$

where $\mathbf{r_p}$ is the coordinate of the hexagonal ring center, and $k_x(k_y)$ is wave number along (perpendicular to) zigzag lines in the junction. The sum runs again over all rings in the junction and a few columns beyond. In Figs. 10(a) and 10(b), we show $F(\boldsymbol{k})$ again for junction I with $N=20$ and $l=6$ close to the zero-conductance point E_2. We see the Bragg peaks at $\mathbf{q_1}=2\pi/a(1/\sqrt{3},\frac{1}{3})$ [or $\mathbf{q_2}=2\pi/a(0,\frac{2}{3})$] and $\mathbf{q_3}=0$,

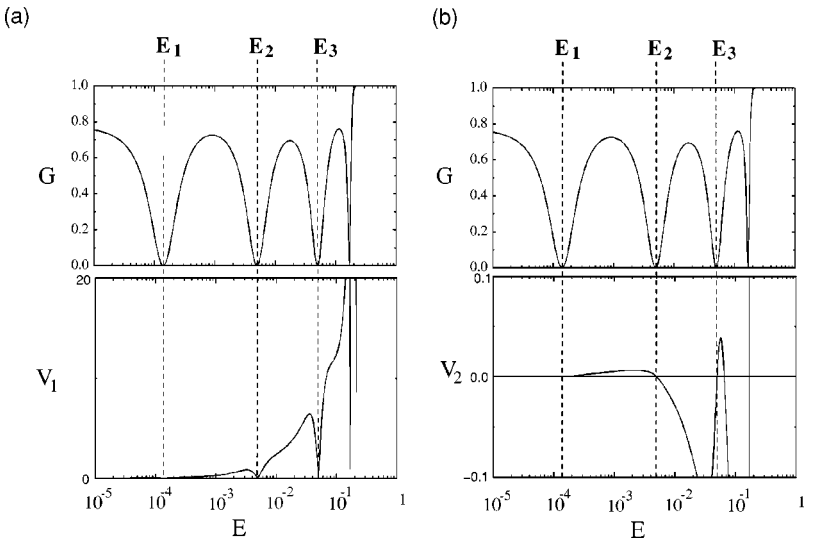

FIG. 9. The Fermi energy dependence of (a) V_1 and (b) V_2, together with the conductance, for the junction I of $N=20$ and $l=6$.

corresponding to a triangular correlation of the flux statelike current vortex pattern depicted in Fig. 8(a). In Fig. 10(c), we show the 3D plot of the $F(\boldsymbol{k})$, where the pronounced triangular symmetry can be observed. We would like to mention here that we have observed analogous current pattern and properties of V_1 and V_2 for junction II.

Finally we would like to draw attention to a remarkable property of the vorticity V_2 (and V_1) close the each zero-conductance point. The net current passing through the junction is defined as

$$J_{\rm net}=(1-|r|^2)J_{\rm lead}=|t|^2J_{\rm lead}, \tag{3.9}$$

where $J_{\rm lead}$ is the incoming component of the current on the source lead line from one of the reservoirs. Close to each zero-conductance point E_n we find $J_{\rm net}\propto(E-E_n)^2$, a quadratic dependence. With the linear dependence of $V_2\propto(E-E_n)$, the total vorticity of the system considered as a ''response'' to a current through the junction ($J_{\rm net}$) diverges as the energy approaches E_i, i.e., $V_2(E)/J_{\rm net}(E)\propto(E-E_n)^{-1}$. Consequently, for energies E close to a zero-conductance point, even a small net current may generate a large vorticity, within the linear response regime. This is not a real linear response, since the external source corresponds to the lead current $J_{\rm lead}$, and the actually measured current $J_{\rm net}$ includes all scattering renormalizations. Nevertheless, the relation between vorticity and transmitted current may be experimentally verified.

E. Negative magnetoresistance

We now consider the effect of an applied magnetic field. It was anticipated above that the zero-conductance resonance should be suppressed by a magnetic field, since it is time reversal symmetry is a condition to realize total reflection. This suggestion is confirmed by our numerical study. For the case of the junction I with $N=20$ and $l=6$, we show the Fermi energy dependence of the conductance in Fig. 11(a),

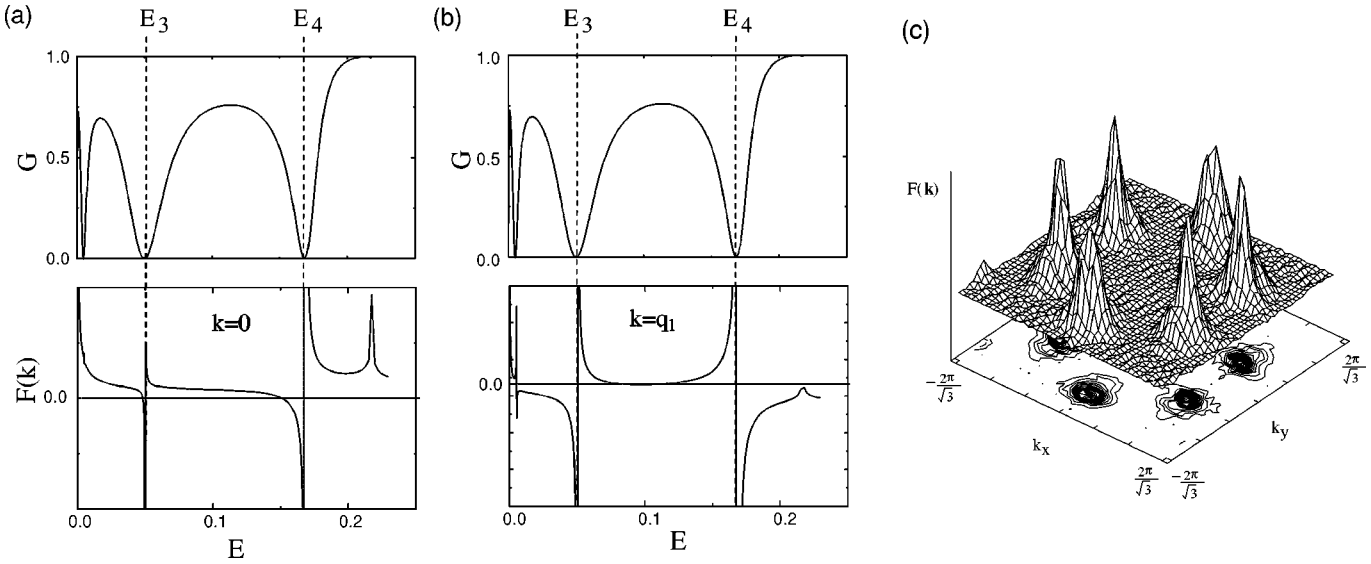

FIG. 10. The Fermi energy dependence of the Fourier transform of the vorticity V_p at (a) $k=0$ and (b) $k=q_1$ for the junction I with $N=20$ and $l=6$. (c) The 3D plot of the correlation of circular current pattern in the M region close to $E=E_2$.

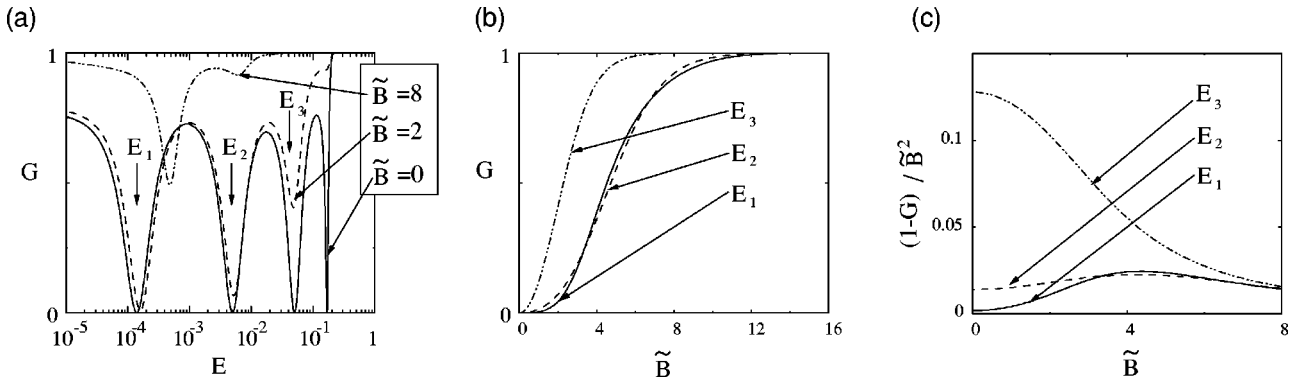

FIG. 11. (a) The Fermi energy dependence of the conductance of the junction I with $N=20$ and $l=6$ when $\tilde{B}=0$ (bold line), $\tilde{B}=2$ (dashed line), and $\tilde{B}=8$ (broken line), within the single channel region. (b) The effective magnetic field dependence of the conductance at $E=E_1$, E_2, and E_3. (c) The plots of $G/\tilde{B}^2$ vs $\tilde{B}$.

where the magnetic field, $\tilde{B}$ is 0, 4, and 16 (scaled with the width of the ribbon as defined in Sec. II). With a finite field the conductance becomes finite and the position of the minimum value of conductance dips moves with increasing the magnetic field. In Fig. 11(b), the magnetic field dependence of the conductance is shown at the energies of $E=E_1$, E_2, and E_3 for the same junction. The indices E_1, E_2, and E_3 specify the energy points of zero-conductance, given in Fig. 11(a). In the very strong field limit, the conductance approaches one in the whole single-channel region. Thus the effect of the magnetic field is not only to removes the zero-conductance dips, but also to turn the system into a perfect conductor, in principle, although it is not possible reach such high fields under experimental conditions.

Figure 11(c) also shows that the coefficient of the quadratic term, i.e., $G=\alpha_0\tilde{B}$, increases with increasing energy E_n. We found a simple law for the dependence connected with the index number n of the zero-conductance dip. The index number n indicates the zero-conductance dip which is associated with s_n state (defined in Sec. III C) at $\tilde{B}=0$. Plotting $l\ln(\alpha_0)$ versus n in Fig. 12, we find linear dependence where the solid (dashed) line represent the data for the junction I with $N=20$ ($N=30$) for $l=6,8,10$. Interestingly, all data have approximately the same slope η. Therefore α_0 follows approximately the exponential behavior

$$\alpha_0 = A(N,l)\exp\left(\eta\frac{n}{l}\right), \tag{3.10}$$

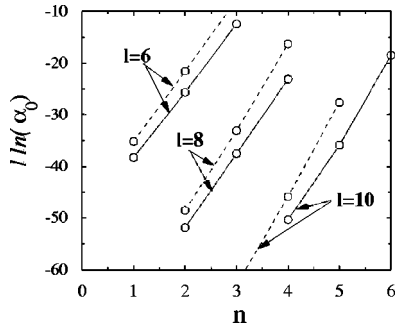

FIG. 12. Scaling properties of magnetoresistance (see text).

where $A(N,l)$ is a factor which depends on l and also weakly on N. This behavior indicates the coupling of the magnetic field increases strongly with increasing index, which is very likely a consequence of the larger overlap of the edge states for increasing E.

IV. CONNECTION WITH ASYMMETRIC AHARANOV-BOHM RING

In this section we discuss the theory of a simple model which has analogous electronic transport properties as the nanographite ribbon junctions on the basis of the scattering matrix theory developed by Büttiker and co-workers.[48] The system analyzed here is the single-channel asymmetric Aharanov-Bohm (AB) ring connected to current leads, as shown in Fig. 13. We will adopt the notation of Ref.48. This system reproduces well the qualitative properties of our ribbon junctions. If the two branches in the AB ring have dif-

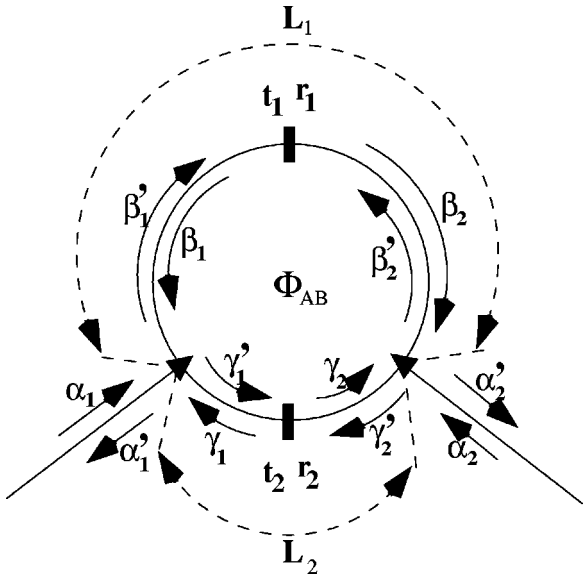

FIG. 13. Schematic figure of Aharanov-Bohm ring, where the definition of the amplitudes of wave functions are written. The length of the upper (lower) branch of the ring is $L_1(L_2)$.

ferent length or different transmission probabilities, zero-transmission resonances appear as a function of energy. A current through the device generates circulating currents in the ring which change sign at each zero-conductance resonance. The application of an external field leading to a finite flux through the ring yield a negative magnetoresistance at the zero-conductance resonance. Finally, we also find that the at the zero-conductance resonance that two branches of the ring possess electron wave function of opposite parity. All these features are common with the nanographite ribbon junctions.

Following the theory developed by Büttiker, we consider the single-channel electron transport through the AB ring as shown in Fig. 13, where the upper and lower branches have different lengths, L_1 and L_2, respectively. The circumference is $L=L_1+L_2=(1+R)L_1$. The notation for the amplitudes of wave functions on the each branch are given in Fig. 13. We assume that each branch has only one conduction channel. The upper(lower)-branch has a scatterer expressed by the transfer matrix t_1 (t_2), which relates the amplitudes to the left to the amplitudes to the right of the scatterers. These transfer matrices are defined as

$$\begin{bmatrix} \beta_2 \\ \beta_2' \end{bmatrix} = \underline{t}_1 \begin{bmatrix} \beta_1' \\ \beta_1 \end{bmatrix} = \begin{bmatrix} 1/t_1^* & -r_1^*/t_1^* \\ -r_1/t_1 & 1/t_1 \end{bmatrix} \begin{bmatrix} \beta_1' \\ \beta_1 \end{bmatrix} \tag{4.1}$$

and

$$\begin{bmatrix} \gamma_1 \\ \gamma_1' \end{bmatrix} = \underline{t}_2 \begin{bmatrix} \gamma_2' \\ \gamma_2 \end{bmatrix} = \begin{bmatrix} 1/t_2^* & -r_2^*/t_2^* \\ -r_2/t_2 & 1/t_2 \end{bmatrix} \begin{bmatrix} \gamma_2' \\ \gamma_2 \end{bmatrix}, \tag{4.2}$$

where $t_i=T_i^{1/2}e^{i\phi_i}$ ($i=1,2$) is the transmission amplitude of the scatterer, T_i the transmission probability, and ϕ_i the phase shift of the transmitted wave ($i=1$ and 2 indicating upper and lower branches, respectively). r_i (r_i') is the reflection amplitude. It is sufficient for our purpose to consider the case where $r_i=0$, i.e., perfect transmission ($T_i=1$).

Now let us consider the junction between lead and ring. The amplitudes of the three outgoing waves are connected with the three incoming ones via a 3×3 scattering matrix (which depends on three parameters only[48]),

$$\begin{bmatrix} \alpha' \\ \beta' \\ \gamma' \end{bmatrix} = \underline{\mathrm{S}} \begin{bmatrix} \alpha \\ \beta \\ \gamma \end{bmatrix} = \begin{bmatrix} -(a+b) & \epsilon^{1/2} & \epsilon^{1/2} \\ \epsilon^{1/2} & a & b \\ \epsilon^{1/2} & b & a \end{bmatrix} \begin{bmatrix} \alpha \\ \beta \\ \gamma \end{bmatrix}, \tag{4.3}$$

where ϵ ($0\leqslant\epsilon\leqslant1/2$) is the key parameter determining the coupling between the ring and a lead. Note that the matrix S is unitary because of the current conservation and symmetric because of the time-reversal invariance. The probability (current) conservation requires that

$$(a+b)^2+2\epsilon=1, \tag{4.4}$$

$$a^2+b^2+\epsilon=1. \tag{4.5}$$

Thus we can rewrite a and b as function of ϵ, e.g., $a_\pm=\pm\frac{1}{2}(\sqrt{1-2\epsilon}-1)$ and $b_\pm=\pm\frac{1}{2}(\sqrt{1-2\epsilon}+1)$.

Now we determine the transmission amplitude and the circulating currents in this system for the arbitrary value of ϵ. The boundary condition are $\alpha_1=1$ and $\alpha_2=0$, i.e., an incident wave from the left lead line. It is straightforward to calculate the amplitude of the transmitted wave

$$\alpha_2' = -e^{-i\theta_1}\frac{\epsilon h}{b^2 \det(\underline{\Pi})}, \tag{4.6}$$

where

$$h=\det(\underline{\Pi})[b-a,1]\underline{t}_1\underline{\Pi}^{-1}\begin{bmatrix} b-a \\ -1 \end{bmatrix}, \tag{4.7}$$

with $\Pi=t_l e^{-i\theta_2}t_2' t_l e^{-i\theta_1}t_1-1$. We have generalized the problem here including the magnetic flux Φ through the loop with $\theta=\theta_1+\theta_2=2\pi\Phi/\Phi_0$. The phase shifts due to the gauge field in the upper and lower branch are $\theta_1=\theta/(1+R)$ and $\theta_2=R\theta/(1+R)$, respectively. The link matrix $\underline{t}_l$ entering in $\underline{\Pi}$ is defined as

$$\begin{bmatrix} \gamma_2' \\ \gamma_2 \end{bmatrix} = \underline{t}_l \begin{bmatrix} \beta_2 \\ \beta_2' \end{bmatrix} = \frac{1}{b}\begin{bmatrix} b^2-a^2 & a \\ -a & 1 \end{bmatrix}\begin{bmatrix} \beta_2 \\ \beta_2' \end{bmatrix}. \tag{4.8}$$

It is also straightforward to obtain the amplitudes in the two branches as follows:

$$\begin{bmatrix} \beta_1' \\ \beta_1 \end{bmatrix} = -\frac{\sqrt{\epsilon}}{b}\underline{\Pi}^{-1}\begin{bmatrix} b-a \\ -1 \end{bmatrix}, \tag{4.9}$$

$$\begin{bmatrix} \gamma_1 \\ \gamma_1' \end{bmatrix} = \frac{\sqrt{\epsilon}}{b}\underline{\tilde{\Pi}}^{-1}\underline{t}_l^{-1}\begin{bmatrix} b-a \\ -1 \end{bmatrix}, \tag{4.10}$$

with $\underline{\tilde{\Pi}}=\underline{t}_l^{-1}e^{i\theta_1}\underline{t}_1^{-1}\underline{t}_l^{-1}e^{i\theta_2}\underline{t'}_2^{-1}-\underline{1}$.

We can then express the transmission amplitude including the finite magnetic flux,

$$\alpha_2'(\Phi,\epsilon)=\frac{i\epsilon(\sin\phi_1+e^{i\theta}\sin\phi_2)}{a^2\cos\gamma\phi+b^2\cos\theta-(1-\epsilon)\cos\phi+i\epsilon\sin\phi}, \tag{4.11}$$

where $\phi=\phi_1+\phi_2$ and $\gamma=(1-R)/(1+R)$. It should be noted that ϕ_1 and ϕ_2 can be written as

$$\phi_1=\frac{1}{1+R}\phi \quad \text{and} \quad \phi_2=\frac{R}{1+R}\phi. \tag{4.12}$$

The transmission probability $T(\Phi,\epsilon)=|\alpha_2'(\Phi,\epsilon)|^2$, proportional to the conductance, shows now zero-conductance dips in the absence of a magnetic field ($\theta=0$). The transmission zeros appear for $\phi=\phi_0$ given by

$$\phi_{0,1}=2m\pi \quad \text{or} \quad \phi_{0,1}=(2m+1)\pi/\gamma, \tag{4.13}$$

where m is an integer.

The resonant behavior of the transmission probability is determined by the poles of the transmission amplitude Eq. (4.11). In order to determine the poles of Eq. (4.11), we

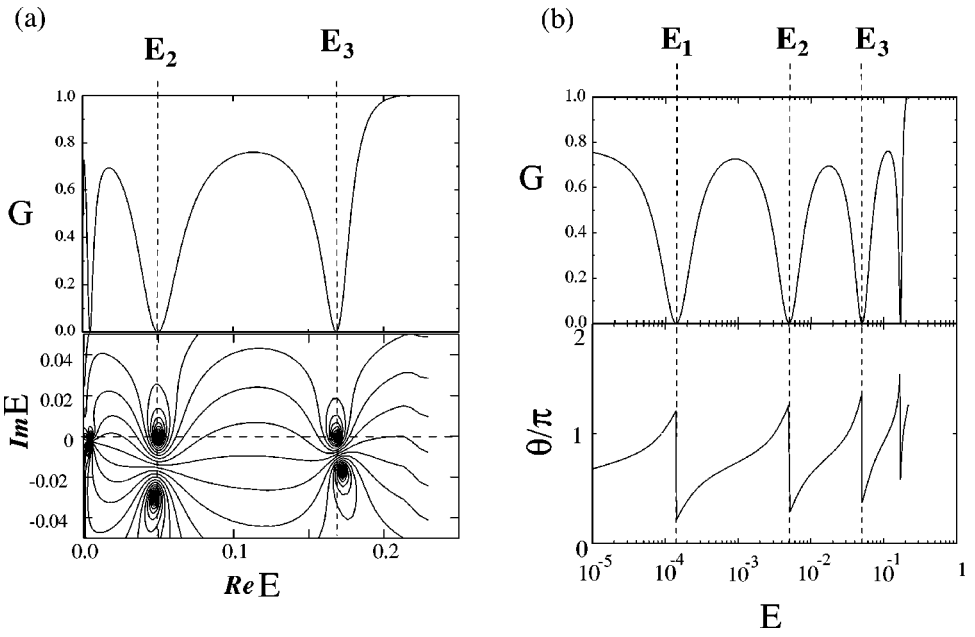

FIG. 14. Numerical results for the junction I with $N=20$ and $l=6$: (a) the contour plot of the absolute value of the transmission amplitude in the complex energy plane. The zero-pole pairs appear at each zero-transmission energy. (b) The energy dependence of the phase of the transmission.

rewrite ϕ as $\phi=\phi_r+i\phi_i$. The real and imaginary part of the phase ϕ are determined by the following two equations:

$$2\sin\gamma\phi_r\sinh\gamma\phi_i-\sin\phi_r[e^{\phi_i}-(1-2\epsilon)e^{-\phi_i}]=0, \tag{4.14}$$

$$a^2\cos\gamma\phi_r\cosh\gamma\phi_i+b^2\cos\theta - \tfrac{1}{2}\cos\phi_r[e^{\phi_i}+(1-2\epsilon)e^{-\phi_i}]=0. \tag{4.15}$$

We can find that one resonance solution is associated with two poles in complex ϕ plane.

In the asymmetric case, i.e., $\gamma\neq 0(R\neq 1)$, it is not easy to deal with Eqs. (4.14) and (4.15) in a simple analytic way. The numerical analysis shows that two types of solutions of zero transmission, $\phi_{0,1}$ and $\phi_{0,2}$, have the following different characteristic features.

(i) $\phi=\phi_{0,1}$ solution. This solution satisfies Eq. (4.11) for arbitrary γ, and gives a zero-transmission resonance which gives in general one zero point and two poles in complex ϕ plane. In the strong coupling limit of $\epsilon=1/2$ with $\gamma\neq 1$, one of two poles goes to infinity, so that the resonance can be characterized by a zero-pole pair in the complex ϕ plane, resulting in the zero-conductance resonance. On the other, when the ring is symmetric i.e., $\gamma=0(R=1)$ for arbitrary coupling, the zero-point and one of two poles are canceled so that only one pole is left on the complex ϕ plane. Then the feature of the resonance is usual resonant transmission due to one pole. Thus the $\phi_{0,1}$ solution gives the condition of anti-resonance for the asymmetric AB-ring system.

(ii) $\phi=\phi_{0,2}$ solution. This solution appears when the ring is asymmetric, i.e., $\gamma\neq 0$. Although this solution also gives a zero point and poles, the zero point and poles are always degenerate on the real axis for arbitrary γ. Therefore the zero-transmission resonance of this solution has different character to that of the $\phi_{0,1}$ solution. The degeneracy of poles and zero point is not lifted by the variation of the coupling parameter ϵ.

In Fig. 14(a), we show the contour plot of the absolute value of the transmission amplitude in the complex energy plane for the junction I with $N=20$ and $l=6$. We can clearly find the zero-pole pair at each zero-conductance energy points. Thus we consider that the nanographite ribbon junction systems corresponds to the asymmetric AB-ring system of strong coupling limit ($\epsilon\rightarrow\frac{1}{2}$). In the strong coupling limit, we can rewrite the transmission probability as

$$T=\left|\alpha_2'\left(\epsilon\rightarrow\frac{1}{2}\right)\right|^2=\frac{4|\sin\phi_1+e^{i\theta}\sin\phi_2|^2}{(\cos\gamma\phi+\cos\theta-2\cos\phi)^2+4\sin\phi}. \tag{4.16}$$

Since the zero-conductance resonances can be characterized by the zero-pole pair on the complex energy plane, one zero-conductance resonance behavior can be written by the following Brite-Wigner form:

$$t_{\mathrm{BW}}(E)=\tilde{t}(E)\frac{E-E_0}{E-(E_p-i\Gamma)}, \tag{4.17}$$

where Γ is the widths of the resonances. E_0 and E_p are the energy of zero and pole, respectively. In general, E_0 is not equal to E_p. When $E_0=E_p$, the resonance have the symmetric Lorentzian form. It is instructive to consider the behavior of the phase of the transmission coefficient θ_{BW}, when $|t_{\mathrm{BW}}|^2$ passes through zero. The phase is defined as

$$\theta_{\mathrm{BW}}=\tan^{-1}\left[\frac{\mathrm{Im}(t_{\mathrm{BW}})}{\mathrm{Re}(t_{\mathrm{BW}})}\right]. \tag{4.18}$$

It is easy to confirm that the phase of the transmission amplitude with the form of Eq. (4.17) jumps at $E=E_0$ (not $E=E_p$) by π.

In Fig. 14(b), the phase of the transmission is depicted, where clear π phase jumps are observed at each conductance energy points. It should be noted that recently the behavior of the phase of transmission coefficient has attracted much interests[49–52] in the context of the experiments by Yacoby *et al.*[53] and Schuster *et al.*[54] It is also mentioned that the appearance of zero-transmission resonances accompanied with the zero-pole pair can be seen not only in the asymmetric AB ring system, but also in the quantum wire system with an attached resonator.[55–62] Thus, the electron transport through the nanographite ribbon junctions is deeply connected to both of them.

Next we consider the circulating current flowing in the AB ring. The electric current on the upper (lower) branch J_1 (J_2) is given by $|\beta_1|^2-|\beta_1'|^2$ ($|\gamma_1'|^2-|\gamma_1|^2$), so that we define the vorticity ($V_{\rm AB}$) of electric currents through the AB ring as J_1+J_2. After the simple mathematical manipulations, we obtain the vorticity $V_{\rm AB}$ as

$$V_{\rm AB}=J_1+J_2 =\frac{2\epsilon b\sin\phi[\sin\gamma\phi+(a+b)\sin\theta]}{[a^2\cos\gamma\phi+b^2\cos\theta-(1-\epsilon)\cos\phi]^2+\epsilon^2\sin^2\phi}. \tag{4.19}$$

In the strong coupling limit ($\epsilon\to 1/2$), we can rewrite the above equation as follows:

$$V_{\rm AB}\left(\epsilon\to\frac{1}{2}\right)=\frac{8\sin\phi\sin\gamma\phi}{[\cos\gamma\phi+\cos\theta-2\cos\phi]^2+4\sin^2\phi}. \tag{4.20}$$

We find that the vorticity $V_{\rm AB}$ changes its sign at the energies of zero-transmission resonances, i.e., $\phi=\phi_0$. At the energies of zero-transmission, the vorticity $V_{\rm AB}$ becomes zero, because no circulating currents can flow at the energies of zero-conductances. Since the expression of the vorticity $V_{\rm AB}$ also has the resonance features, the vorticity becomes stronger around the energies of zero-transmission resonances. These behaviors of the vorticity are consistent with our numerical calculation results on the nanographite junctions.

Now we consider the parity of the wave functions at the energies of zero transmission. In order to discuss the behavior of the wave functions in the AB ring, let us construct the wave functions in the AB-ring as follows:

$$\Psi(x)=\begin{cases}\beta_1 e^{ik^+x}+\beta_1' e^{-ik^-x} & -L_1\leqslant x\leqslant 0,\\ \gamma_1' e^{ik^+x}+\gamma_1 e^{-ik^-x} & 0\leqslant x\leqslant L_2,\end{cases} \tag{4.21}$$

where the origin of x is the left junction and $k^\pm=k\pm\theta/L$. Another expression of the wave functions is

$$\tilde{\Psi}(\tilde{x})=\begin{cases}\beta_2' e^{ik^+\tilde{x}}+\beta_2 e^{-ik^-\tilde{x}} & 0\leqslant\tilde{x}\leqslant L_1,\\ \gamma_2 e^{ik^+\tilde{x}}+\gamma_2' e^{-ik^-\tilde{x}} & -L_2\leqslant\tilde{x}\leqslant 0,\end{cases} \tag{4.22}$$

where the origin of $\tilde{x}$ is the right junction. In the following, we use the former wave functions. For $\phi_0=2m\pi$, we can easily derive the asymptotic form of the wave functions near $x=0$,

$$\Psi(\delta)=(A^2+A^{-2})^2+(A^2+A^{-2})\delta, \quad \text{for the upper branch}, \tag{4.23}$$

$$\Psi(-\delta)=(A^2+A^{-2})^2-(A^2+A^{-2})\delta, \quad \text{for the lower branch} \tag{4.24}$$

and near $x=-L_1$ and L_2,

$$\Psi(-L_1+\delta)=2(A-A^{-1})\delta, \quad \text{for the upper branch}, \tag{4.25}$$

$$\Psi(L_2-\delta)=-2(A-A^{-1})\delta, \quad \text{for the lower branch}, \tag{4.26}$$

where δ is infinitesimal value $A=e^{im\gamma\pi}$. We should note that at the energy of the zero-transmission, i.e., $\phi=\phi_0$, the wave function form the standing wave along the ring, in which the node of wave function appears at the right junction. We can also find that the wave function on the upper branch has m nodes, and the the wave function on the lower branch has $(m+1)$ nodes, so that the wave functions of the upper (lower) branch has the opposite parity at the energies of zero transmission. Actually looking at Fig. 7, in the nanographite ribbon junctions, the wave function along the zigzag edge and the wave function along the bearded edge have always different parity.

The zero-conductance resonance is a consequence of the destructive time-reversal interference. The application of magnetic field can destroy these zero-transmission resonances, resulting in the negative magnetoresistances. For the weak magnetic field limits ($\theta\ll 1$), we can easily derive the magnetic field dependence of the transmission probability as follows:

$$T(\theta)=\left[\frac{\sin(m\gamma\pi)}{a^2\cos(2m\gamma\pi)+b^2+\epsilon-1}\right]\theta^2+O(\theta^3) \quad \text{at} \quad \phi_0=2m\pi, \tag{4.27}$$

$$T(\theta)=\left[\frac{\cos^2[(2m+1)\pi/2\gamma]}{\{a^2+b^2-(1-\epsilon)\cos[(2m+1)\pi/\gamma]\}^2+\epsilon^2\sin^2[(2m+1)\pi/\gamma]}\right]\theta^2+O(\theta^3), \quad \text{at} \quad \phi_0=(2m+1)\pi/\gamma. \tag{4.28}$$

For both cases, the zero transmission is removed in the form of θ^2.

In the summary of this section, we have shown the connection between the electron transport through nanographite ribbons and the electron transmission through the asymmetric Aharanov-Bohm ring system. We could understand that the zero-conductance resonances are the interference effect of two transmission paths split in the scattering region of the nanographite ribbon junctions. The interference effects can be visualized by the formation of the standing waves whose parity is different at two edges in the junctions, and the circulating currents with Kékule-like vortex pattern. The results presented here will be the basis of the phenomenological theory on nanographite junction systems remained for future study.

V. SUMMARY AND DISCUSSION

This paper presented the electronic transport properties through nanographite ribbon junctions connecting two zigzag ribbons with same or different width by the Landauer-Büttiker approach using a tight-binding model. The zigzag shape of graphite edge provide a nonbonding edge localized state at $E=0$. A single edge state cannot contribute the electron transport due to this nonbonding character, however, in the zigzag ribbon systems the bonding and antibonding configuration between two edge states can provide a single conducting channel. Our numerical analyses have shown that the electrical conductance of nanographite ribbon junctions crucially depends on their morphology and edge shapes.

In the single-channel conducting region, the Fermi energy dependence of electrical conductance of nanographite ribbon junctions shows rich structures with sharp zero-conductance dips. We analyzed the origin of the zero-conductance dips from the behavior of electron waves and electric currents. Each zero-conductance resonance can be associated with a quasibound state in the scattering region of the junctions, yielding the formation of standing waves. It is also found that in the scattering region the electron waves are split into two edge localized electron waves which have opposite parity each other.

Furthermore, when the energy of the incident electron waves is close to the energy of zero conductance resonances, the electric currents form the circulating currents with a Kekulé-like vortex pattern in the scattering region. This electric current behaviors resemble flux states in the sense that they show a strong current-current correlation. The flux states strongly appears in the scattering region, and rapidly decreases with leaving from the scattering region. This circulating currents changes the its direction as we cross the energies of the zero-conductance dip. Therefore, the zero-conductances are caused by the superposition of two flux states with opposite chirality, resulting in the formation of standing waves.

We have presented not only the numerical analysis, but also the phenomenological theory for the zero-conductance resonances associated with the electric current vortex. It was pointed out that the single-channel transport through the nanographite ribbon junctions can be connected to the physics of the asymmetric Aharanov-Bohm ring system. The zero-conductance resonance is the consequence of the destructive interference effects between two conducting-channels in the scattering region which is split from the single-conducting channel of edge states. The analysis in the complex energy plane shows the Brite-Wigner form of Eq. (4.17). This means that the zero-conductance resonance can be viewed as so-called Fano resonances,[63] which are known to occur when two scattering channels are available, one corresponding to a continuum of states and the other to a discrete quasibound state. It also is known that the Fano resonances can be occurred in the quantum wire with a *t*-stub resonator.[57,58] Thus, the single-channel electron transport through nanographite ribbon junctions has the similarities not only to the asymmetric Aharanov-Bohm ring, but also to the quantum wire with a *t*-stub resonator.

The zero-conductance resonances are the consequence of the time-reversal symmetry of the system. The application of a magnetic field removes these zero-conductance dips, yielding a pronounced negative magneto resistance. Since carbon nanotubes show the large positive magnetoresistance, the negative magnetoresistance in nanographite systems is contrast.

Theoretically, there is a deep connection between the appearance of flux states and the problem of chiral anomaly in the $(2+1)$-dimensional system of fermions. Semenoff[64] have pointed out that the K and K' point of graphite have a different chirality. This chiral feature of graphite lattice appears if there is an imbalance between the two sublattices of graphite lattice, e.g., by different onsite potential. The edge states on zigzag edges are a consequence of this imbalance, since the most outer sites belong to a single sublattice. The abrupt change of the sublattice on the edge as it occurs for the nanographite junctions yields the boundary condition to form the degenerate flux states in the scattering-region of the junctions. From our numerical analysis no further obvious rules for the creation of localized flux states can be derived. The detailed analysis between chiral features of graphite and the flux states will be given elsewhere.

Since the nonmagnetic potential impurity or a lattice vacancy can also induce the imbalance between sublattices, these lattice defects can induce the conductance zeros accompanied with the flux states.[23,65,66] The energy levels of zero conductances corresponds to the quasibound state energy level. The energy levels of the conductance zeros depends on the strength of overlapping between edge states and the impurity state. Quantitative analysis is given elsewhere.

VI. CONCLUSION

In conclusion, we numerically analyzed the electrical transport properties of nanographite junctions based on the tight-binding model. We found that the conductance of various junctions having zigzag edges shows a very rich structure as a function of the energy (chemical potential) with

many zero-conductance dips in the low-energy region. These dips are identified as resonances connected with twofold degenerate flux states which form circular-current Kekulé patterns. It is obvious that the topology of the edges is crucial for this phenomenon and the chirality connected with the sublattice structure plays an important role. The degeneracy of states responsible for the resonances can be lifted by a magnetic field, leading to negative magneto resistance. While the structures used in the calculation might be difficult to produce at present, our results also suggest that transport properties of defective carbon nanotubes, carpet-roll, or papier-mâché structures[28] could be rather different from the transport properties of usual multiwall nanotubes or SWCN which have only weak features in the single-channel regime. The present study not only clarifies the importance of the edges and their shapes on transport properties, but also indicates the necessity of further theoretical studies to explicate the interplay between the transport properties and the network topology of carbon atoms.

ACKNOWLEDGMENTS

The authors are grateful to T. Arima, T. Enoki, A. Furusaki, M. Igami, K. Kusakabe, K. Nakada, K. Nakao, S. Okada, C. Oshima, M. Sigrist, Y. Takagi, K. Takita, K. Terakura, H. Tsunetsugu, T. Uda, and the late M. Fujita for many helpful discussions. K.W. acknowledges the hospitality of the Jonint Research Center for Atom Technology (JRCAT). He also acknowledges the financial support of the Japan Society for the Promotion of Science for Young Scientist. This work was supported partly by Grants-in-Aid for Scientific Research No. 10309003 and 10640341 from the Ministry of Education, Science and Culture, Japan. K.W is also grateful for the financial support from the Foundation Advanced Technology institute and from the Kinki-chihou Hatsumei Center. Numerical calculations were performed in part on VPP500 in Institute for Solid State Physics, University of Tokyo, on SX5 in Institute for Molecular Science, and on computers in Yukawa Institute for Theoretical Physics, Kyoto University.

*Left from Yukawa Institute for Theoretical Physics, Kyoto University and Institute of Materials Science, University of Tsukuba.

[1] Y. Imry, *Introduction to Mesoscopic Physics* (Oxford University Press, Oxford, 1997); S. Datta, *Electronic Transport in Mesoscopic Systems* (Cambridge University Press, Cambridge 1995).

[2] R. P. Feynman, Science **254**, 1300 (1991); L. Kouwenhoven, *ibid.* **275**, 1896 (1997).

[3] M. S. Dresselhaus, G. Dresselhaus, and P. C. Eklund, *Science of Fullerenes and Carbon Nanotubes* (Academic Press, San Diego, 1996).

[4] R. Saito, G. Dresselhaus, and M. S. Dresselhaus, *Physical Properties of Carbon Nanotubes* (Imperial College Press, London, 1998).

[5] J. W. G. Wildöer, L. C. Venema, A. G. Rinzler, R. E. Smalley, and C. Dekker, Nature (London) **391**, 59 (1998); T. W. Odom, J. Huang, P. Kim, and C. M. Lieber, *ibid.* **391**, 62 (1998).

[6] P. L. McEuen, M. Bockrath, D. H. Cobden, Y. Yoon, and S. G. Louie, cond-mat/9906055; C. Dekker, Phys. Today **52**, 22 (1999), for reviews.

[7] M. Bockrath, D. H. Cobden, P. L. McEuen, N. G. Chopra, A. Zettl, A. Thess, and R. E. Smalley, Science **275**, 1922 (1997).

[8] A. Bezryadin, A. R. M. Verschueren, S. J. Tans, and C. Dekker, Phys. Rev. Lett. **80**, 4036 (1998).

[9] S. J. Tans, M. H. Devoret, H. Dai, A. Thess, R. E. Smalley, L. J. Geerligs, and C. Dekker, Nature (London) **386**, 474 (1997).

[10] Z. Yao, H. W. C. Postma, L. Balents, and C. Dekker, Nature (London) **402**, 273 (1999).

[11] S. Frank, P. Poncharal, Z. L. Wang, and W. A. De Heer, Science **280**, 1744 (1998).

[12] K. Tsukagoshi, B. W. Alphenaar, and H. Ago, Nature (London) **401**, 572 (1999).

[13] A. F. Morpurgo, J. Kong, C. M. Marcus, and H. Dai, Science **286**, 263 (1999).

[14] T. Ando and T. Nakanishi, J. Phys. Soc. Jpn. **67**, 1704 (1998); T. Ando, T. Nakanishi, and R. Saito, *ibid.* **67**, 2857 (1998).

[15] Yu. A. Krotov, D.-H. Lee, and S. G. Louie, Phys. Rev. Lett. **78**, 4245 (1997); C. Kane, L. Balents, and M. P. A. Fisher, *ibid.* **79**, 5086 (1997); R. Egger and A. O. Gogolin, *ibid.* **79**, 5082 (1997); H. Yoshioka and A. A. Odintsov, *ibid.* **82**, 374 (1999).

[16] L. Chico, M. P. L. Sancho, and M. C. Muoz, Phys. Rev. Lett. **81**, 1278 (1998); L. Chico, V. H. Crespi, L. X. Benedict, S. G. Louie, and M. L. Cohen, *ibid.* **76**, 971 (1996).

[17] R. Tamura and M. Tsukada, Phys. Rev. B **55**, 4991 (1997).

[18] H. Matsumura and T. Ando, J. Phys. Soc. Jpn. **67**, 3542 (1998).

[19] R. Tamura and M. Tsukada, Phys. Rev. B **58**, 8120 (1998).

[20] M. Igami, T. Nakanishi, and T. Ando, J. Phys. Soc. Jpn. **68**, 716 (1999).

[21] M. Fujita, K. Wakabayashi, K. Nakada, and K. Kusakabe, J. Phys. Soc. Jpn. **65**, 1920 (1996); Recently Takagi and co-workers have extented the idea of the edge states and proposed a series of networks with edge states (Ref. 22). The connection between the edge states and Andreev bound states of anisotropic superconductivity is also discussed in Ref. 23.

[22] Y. Takagi, M. Fujita, K. Wakabayashi, M. Igami, S. Okada, K. Nakada, and K. Kusakabe, cond-mat/0001027; Y. Takagi, M. Fujita, and K. Kusakabe, Mol. Cryst. Liq. Cryst. Sci. Technol., Sect. A **340**, 379 (2000).

[23] K. Wakabayashi, Ph.D. thesis, University of Tsukuba, 2000.

[24] K. Nakada, M. Fujita, G. Dresselhaus, and M. S. Dresselhaus, Phys. Rev. B **54**, 17 954 (1996).

[25] K. Wakabayashi, M. Fujita, H. Ajiki, and M. Sigrist, Phys. Rev. B **59**, 8271 (1999).

[26] Note that graphite ribbons can be a simple model of defective carbon nanotubes of carpet-roll or papier-mâché forms (Ref. 28) activated carbon fibers (Refs. 29–31), and graphitized nanodiamond particles (Ref. 32). There are also some trials to fabricate nanographite ribbons on metal substrates (Ref. 33), or fabrications by STM (Ref. 34).

[27] K. Wakabayashi, M. Fujita, and M. Sigrist, J. Phys. Soc. Jpn. **67**, 2089 (1998).

[28] O. Zhou, R. M. Fleming, D. W. Murphy, C. H. Chen, R. C. Haddon, A. P. Ramirez, and S. H. Glarum, Science **263**, 1744 (1994); S. Amelinckx, D. Bernaerts, X. B. Zhang, G. V. Tendeloo, and J. V. Landuyt, *ibid.* **267**, 1334 (1995).

[29] A. W. P. Fung, M. S. Dresselhaus, and M. Endo, Phys. Rev. B **48**, 14 953 (1993); A. Nakayama, K. Suzuki, T. Enoki, S. L. di Vittorio, M. S. Dresselhaus, K. Koga, M. Endo, and N. Shindo, Synth. Met. **55-57**, 3736 (1993); A. W. P. Fung, Z. H. Wang, M. S. Dresselhaus, G. Dresselhaus, R. W. Pekala, and M. Endo, Phys. Rev. B **49**, 17 325 (1994); A. Nakayama, K. Suzuki, T. Enoki, K. Koga, M. Endo, and N. Shindo, Bull. Chem. Soc. Jpn. **69**, 333 (1996); Y. Shibayama, H. Sato, T. Enoki, and M. Endo, Phys. Rev. Lett. **84**, 1744 (2000).

[30] M. S. Dresselhaus, G. Dresselhaus, K. Sugihara, I. L. Spain, and H. A. Goldberg, *Graphite Fibers and Filaments* (Springer-Verlag, Berlin, 1988).

[31] *Supercarbon*, edited by S. Yoshimura and R. P. H. Chan (Springer-Verlag, Berlin, 1998).

[32] O. E. Andersson, B. L. V. Prasad, H. Sato, T. Enoki, Y. Hishiyama, Y. Kaburagi, M. Yoshikawa, and S. Bandow, Phys. Rev. B **58**, 16 387 (1998).

[33] M. Terai, N. Hasegawa, M. Okusawa, S. Otani, and C. Oshima, Appl. Sur. Sci. **130-132**, 876 (1998); C. Oshima (private communication).

[34] T. W. Ebbesen, and H. Hiura, Adv. Mater. **7**, 582 (1995); H. Hiura, T. W. Ebbesen, J. Fujita, K. Tanigaki, and T. Takada, Nature (London) **367**, 148 (1994); H. Hiura (private communication).

[35] Y. Miyamoto, K. Nakada, and M. Fujita, Phys. Rev. B **59**, 9858 (1999); **60**, 16211(E) (1999).

[36] P. W. Anderson, D. J. Thouless, E. Abrahams, and D. S. Fisher, Phys. Rev. B **22**, 3519 (1980).

[37] M. Büttiker, Y. Imry, R. Landauer, and S. Pinhas, Phys. Rev. B **31**, 6207 (1985).

[38] R. Landauer, Z. Phys. B **68**, 217 (1987).

[39] A. MacKinnon, Z. Phys. B **59**, 385 (1985).

[40] T. Ando, Phys. Rev. B **44**, 8017 (1991).

[41] K. Wakabayashi, and M. Sigrist, Phys. Rev. Lett. **84**, 3390 (2000).

[42] P. R. Wallace, Phys. Rev. **71**, 622 (1947).

[43] R. Saito, M. Fujita, G. Dresselhaus, and M. S. Dresselhaus, Appl. Phys. Lett. **60**, 2204 (1992).

[44] R. Saito, M. Fujita, G. Dresselhaus, and M. S. Dresselhaus, Phys. Rev. B **46**, 1804 (1992).

[45] R. Peierls, Z. Phys. **80**, 763 (1933).

[46] The zigzag (bearded) ribbons at $k=2\pi/3a$ can be mapped to a finite one-dimensional chain with $2N$ $(2N+1)$ sites, which can be solved analytically (see the appendix of Ref. 25). From this analytic solution, the form of Δ_z (Δ_b) is easily derived.

[47] S. Nakanishi and M. Tsukada, Jpn. J. Appl. Phys. **37**, 3805 (1998).

[48] M. Büttiker, Y. Imry, and M. Ya. Azbel, Phys. Rev. A **30**, 1982 (1984).

[49] P. S. Deo, and A. M. Jayannavar, Mod. Phys. Lett. B **10**, 787 (1996).

[50] C.-M. Ryu and S. Y. Cho, Phys. Rev. B **58**, 3572 (1998).

[51] H.-W. Lee, Phys. Rev. Lett. **82**, 2358 (1999).

[52] T. Taniguchi and M. Büttiker, Phys. Rev. B **60**, 13 814 (1999).

[53] A. Yacoby, M. Heiblum, D. Mahalu, and H. Shtrikman, Phys. Rev. Lett. **74**, 4047 (1995).

[54] R. Schuster, E. Buks, M. Heiblum, D. Mahalu, V. Umansky, and H. Shtrikman, Nature (London) **385**, 417 (1997).

[55] P. S. Deo and A. M. Jayannavar, Phys. Rev. B **50**, 11 629 (1994).

[56] R. Sordan and K. Nikolić, Phys. Rev. B **52**, 9007 (1995).

[57] Z. Shao, W. Porod, and C. S. Lent, Phys. Rev. B **49**, 7453 (1994).

[58] W. Porod, Z. Shao, and C. S. Lent, Phys. Rev. B **48**, 8495 (1993); W. Porod, Z. Shao, and C. S. Lent, Appl. Phys. Lett. **61**, 1350 (1992).

[59] J. Wang, Y. Wang, and H. Guo, Appl. Phys. Lett. **65**, 1793 (1994).

[60] F. Sols, M. Macucci, U. Ravaioli, and K. Hess, J. Appl. Phys. **66**, 3892 (1989).

[61] H. Xu and W. Sheng, Superlattices Microstruct. **25**, 79 (1999).

[62] H. Xu and W. Sheng, Phys. Rev. B **57**, 11 903 (1998).

[63] U. Fano, Phys. Rev. **124**, 1866 (1961).

[64] G. W. Semenoff, Phys. Rev. Lett. **53**, 2449 (1984).

[65] K. Wakabayashi and M. Sigrist, Synth. Met. **121**, 1231 (2001).

[66] K. Wakabayashi and M. Sigrist, in *Proceedings of the 25th International Conference on Physics and Semiconductors, Osaka, 2000*, edited by N. Miura and T. Ando (Springer, New York, 2001), p. 1643.